



High-Precision Ringdown Surrogate Model for Non-Precessing Binary Black Holes

Lorena Magaña Zertuche ^{1,*}, Leo C. Stein ¹

Keefe Mitman ², Scott E. Field ^{3,4}, Vijay Varma ³, Michael Boyle ⁵, Nils Deppe ^{6,7,5}, Lawrence E. Kidder ⁵, Jordan Moxon ², Harald P. Pfeiffer ⁸, Mark A. Scheel ², Kyle C. Nelli ², William Throwe ⁵ and Nils L. Vu ²

¹*Department of Physics and Astronomy, University of Mississippi, University, Mississippi 38677, USA*

²*Theoretical Astrophysics 350-17, California Institute of Technology, Pasadena, California 91125, USA*

³*Department of Mathematics and Center for Scientific Computing & Visualization Research, University of Massachusetts, Dartmouth, MA 02747*

⁴*Department of Physics and Center for Computational Research, East Hall, University of Rhode Island, Kingston, RI 02881*

⁵*Cornell Center for Astrophysics and Planetary Science, Cornell University, Ithaca, New York 14853, USA*

⁶*Laboratory for Elementary Particle Physics, Cornell University, Ithaca, New York 14853, USA*

⁷*Department of Physics, Cornell University, Ithaca, New York 14853, USA*

⁸*Max Planck Institute for Gravitational Physics (Albert Einstein Institute), Am Mühlenberg 1, Potsdam 14476, Germany*

(Dated: August 13, 2024)

Highly precise and robust waveform models are required as improvements in detector sensitivity enable us to test general relativity with more precision than ever before. In this work, we introduce a spin-aligned surrogate ringdown model. This ringdown surrogate, `NRSur3dq8_RD`, is built with numerical waveforms produced using Cauchy-characteristic evolution. In addition, these waveforms are in the superrest frame of the remnant black hole allowing us to do a correct analysis of the ringdown spectrum. The novel prediction of our surrogate model is complex-valued quasinormal mode (QNM) amplitudes, with median relative errors of $10^{-2} - 10^{-3}$ over the parameter space. Like previous remnant surrogates, we also predict the remnant black hole’s mass and spin. The QNM mode amplitude errors translate into median errors on ringdown waveforms of $\sim 10^{-4}$. The high accuracy and QNM mode content provided by our surrogate will enable high-precision ringdown analyses such as tests of general relativity. Our ringdown model is publicly available through the python package `surfinBH`.

I. INTRODUCTION

After the cataclysmic collision of two black holes, the remnant black hole vibrates at different frequencies in what is known as the ringdown phase. These quasinormal mode (QNM) frequencies are dictated by the mass and spin of the final black hole. Understanding the corresponding amplitudes of these QNMs allows us to model the aftermath of a binary black hole (BBH) merger [1–4]. However, to estimate the QNM amplitudes, we must rely on numerical relativity (NR) waveforms. Yet producing a single numerical relativity waveform describing a specific BBH system is computationally expensive and can take weeks to months to run. An additional layer of complication is added due to the large BBH parameter space — consisting of both BH masses and spin vectors among other parameters. Due to this, it is challenging to densely populate the full parameter space with NR waveforms and, therefore, it presents a difficulty for accurate parameter inference with current ground-based detectors.

Nevertheless, there are several BBH waveform models that help ameliorate this problem. A popular framework used in dealing with the general-relativistic two-body problem is the effective-one-body, or EOB, approach. It allows one to model the full BBH evolution by including both perturbative results from the inspiral and ringdown phases as well as the full NR solution from the merger [5, 6].

An alternative way to generate waveforms is to use phenomenological models to aid in detection and parameter inference. Although these models are fast, they use several approximations which not only affect parameter estimation but also limit the area of parameter space they can cover [7, 8]. To mitigate these issues, several groups have turned to the use of surrogate modelling [9–12]. This type of modelling uses machine learning regression techniques informed by NR simulations. One must first build an accurate basis using the NR waveforms and then interpolate to construct new waveform templates in areas of parameter space not covered by simulations [13].

In this work, however, we take a different approach. We build a ringdown surrogate model, `NRSur3dq8_RD`, similar in methodology to [10]. We use Gaussian process regression (GPR), a supervised, machine learning algorithm, to interpolate between existing simulation data so that we can model a ringdown waveform at any point in parameter space. In other words, we do not need to directly model waveforms for all of the parameter space. Instead, we make a map from BBH system parameters like initial masses and spins to the remnant parameters of mass, spin, and complex QNM mode amplitudes. This surrogate model allows us to make predictions for systems with parameters that have not been simulated. More specifically, these systems have their spins aligned with the system’s orbital angular momentum. We fit for the QNM amplitudes at a time $20M$ after the peak of the L^2 -norm of the waveform, or $u_0 = u_{\text{peak}} + 20M$, and use those to build our model. Here, u_0 is defined as freely-specified

* lmaganaz@go.olemiss.edu

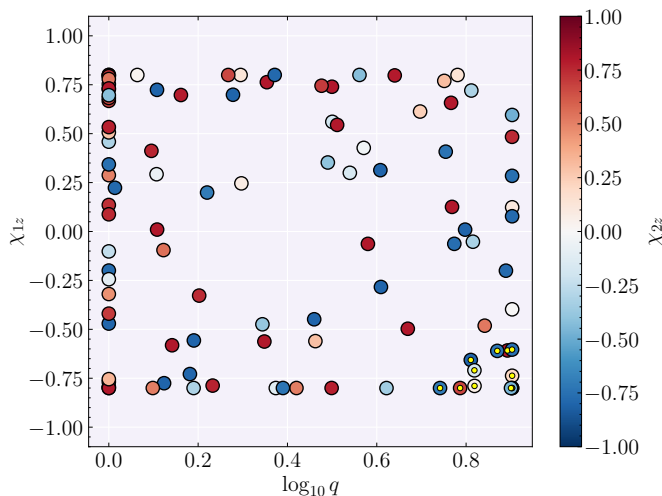


FIG. 1. The parameter space spanned by the 102 NR simulations we use to build `NRSur3dq8_RD`. These are the same NR simulations used in surrogates `NRHybSur3dq8` and `NRHybSur3dq8_CCE` [13, 19]. The axes show the spin on the heavier black hole versus the common logarithm of the mass ratio while the colorbar indicates the spin on the lighter black hole. The yellow dots inside the circles (bottom right corner) are those simulations with a larger retrograde (2, 2, 0) mode than the prograde mode.

start time of the model. The QNM fitting algorithm is the same used in previous work [14].

The strength of our approach relies on the inclusion of multiple QNMs, memory, and the use of the correct Bondi-van der Burg-Metzner-Sachs (BMS) frame in our simulations, i.e., the superrest frame of the remnant BH [15–18]. The inclusion of memory and BMS frame fixing allows us to extract more accurate QNM amplitudes as well as more precisely model the ringdown portion of the waveform [14, 19].

The LIGO-Virgo-KAGRA detector network has already observed ringdown-dominated signals, such as GW190521 [20]. Soon, third-generation, ground-based detectors such as Cosmic Explorer (CE), the Einstein Telescope (ET), and space-based detectors such as the Laser Interferometer Space Antenna (LISA), will detect thousands of ringdown signals rich in QNM content [21–25]. Future detections require quick and robust modelling, which allows us to perform more accurate parameter estimation. However, existing surrogates perform poorly in the ringdown portion of a waveform. Therefore, we introduce aligned-spin ringdown surrogate `NRSur3dq8_RD`. This new model is publicly available through the python package `surfinBH` [10, 26].

The paper is organized as follows. In Sec. II we cover QNM conventions used throughout this work. In Sec. III we discuss the main challenges of performing QNM amplitude fits. Then in Sec. IV, we introduce Gaussian process regression as our machine learning algorithm of choice. We also present the waveform simulations used and the

methods for training and testing the ringdown surrogate model. Finally, in Sec. V we discuss model performance and results and comment on future work in Sec. VI.

II. QNM CONVENTIONS

Each complex QNM frequency, ω , is labelled by numbers (ℓ, m, n) where (ℓ, m) correspond to the angular numbers and $n = 0, 1, \dots$ is an overtone number. Stable mode solutions live in the lower half-plane i.e., $\text{Im}[\omega] < 0$, and there is additional symmetry between the left and right half-planes such that $-\omega_{\ell, -m}^*$ is the mirror mode of $\omega_{\ell, m}$ [27–31]. Therefore, modes where $\text{Re}[\omega] > 0$ are known as “ordinary” and those with $\text{Re}[\omega] < 0$ are “mirror” modes.

In addition to this symmetry, each QNM frequency has two solutions denoted by the superscript p : one solution that is co-rotating with the BH, or prograde ($p = +1$), and another counter-rotating with the BH, called retrograde ($p = -1$). We call a mode prograde if $\text{sgn}(m) = +\text{sgn}(\text{Re}[\omega])$ and retrograde if $\text{sgn}(m) = -\text{sgn}(\text{Re}[\omega])$, following the naming convention of [14]. This nomenclature breaks down for cases where $m = 0$, where neither of the two solutions are known to be dominant.

Putting the above information together, we express a ringdown waveform as

$$h^Q(u, \theta, \phi) = \sum_{\ell', m, n, p} \left[\mathcal{A}_{\ell' m n}^p e^{-i\omega_{\ell' m n}^p (u - u_{\text{ref}})} \sum_{\ell} C_{\ell \ell' m} (a\omega_{\ell' m n}^p) {}_{-2}Y_{\ell m}(\theta, \phi) \right], \quad (1)$$

where the $\mathcal{A}_{\ell' m n}^p$ are complex amplitudes for each QNM, $\omega_{\ell' m n}^p$ are the QNM frequencies, $C_{\ell \ell' m} (a\omega_{\ell' m n}^p)$ are called the spherical-spheroidal mixing coefficients in the conventions of [32, 33], and ${}_{-2}Y_{\ell m}(\theta, \phi)$ are the spin-weight -2 spherical harmonic functions. Here, $a = |J|/M$ is the BH spin parameter while θ and ϕ represent the usual polar and azimuthal angles. The QNM model vanishes for times earlier than the start time, $h(u < u_0) = 0$. The mode amplitudes are specified at a time u_{ref} . Almost everywhere we will choose $u_{\text{ref}} = u_0$, except when testing for stability of mode amplitudes.

III. CHALLENGES IN QNM FITTING

Building a ringdown surrogate model requires at least a couple of important choices to be made. The first is choosing a QNM model start time u_0 for fitting the QNM amplitudes. Since there is no clear time when the merger ends and ringdown begins, we cannot prematurely choose the time when the waveform amplitude peaks to perform our fits. A second challenge is to pick the number of modes that we want to include in the surrogate model. Since different modes are important for different configurations

of BBH systems, it is more complex than choosing the 10 loudest modes of a single simulation.

A. On Choosing the Modes

To answer these questions, we evaluate which QNM amplitudes are the most important in each simulation. Apart from aligning the peaks of the L^2 norm of the waveforms to be $u_{\text{peak}} = 0 M$, it is important to note that there is rotational freedom around the \hat{z} -direction. Therefore, we can choose which $U(1)$ rotation to perform on these spin-aligned systems so that a better comparison can be made between simulations. Our choice is to make the $(\ell, m) = (2, 2)$ spherical mode be real and positive at $u = u_0$. We then proceed to fit for all 168 QNM amplitudes ($\ell = 2 - 4, |m| \leq \ell, n = 0 - 7$) for each simulation at times $u_0 - u_{\text{peak}} \in [-10M, 50M]$. This range in times allows us to evaluate how the absolute amplitudes evolve and which ones are the loudest in each simulation. It turns out that although the mode order varies between simulations, they have the most important modes in common. From this analysis, we also notice that in a handful of the simulations, the amplitude of the retrograde mode is dominant over the prograde mode amplitude. This remains true whether one fits for all 168 modes or the 20 loudest modes. The simulations for which this occurs are denoted by a yellow dot on Fig. 1. Through this figure, one can see that the retrograde mode dominates in a certain area of parameter space, i.e., only for systems with a high mass ratio ($q \gtrsim 5.5$) and a high primary spin that is aligned with the $-\hat{z}$ direction, i.e., negatively spinning.

B. On Choosing the Fitting Times

To understand the fitting times, we constrain the number of modes we fit to a set of 26 modes: $(2, \pm 2, 0, \pm)$, $(2, \pm 2, 1, \pm)$, $(2, \pm 1, 0, \pm)$, $(2, 0, 0, \pm)$, $(3, \pm 3, 0, \pm)$, $(3, \pm 2, 0, \pm)$, and $(4, \pm 4, 0, \pm)$. Unlike the conventions in [14], here we define an individual mode to include only the prograde or retrograde solution such as $(\ell, |m|, n, +)$ or $(\ell, |m|, n, -)$, respectively. However, note that for building the surrogate mode we use a subset of the modes above, as seen in Sec. IV A. We fit the QNM amplitudes for times $u_0 - u_{\text{peak}} \in [-10M, 100M]$ to evaluate which time or range in time is the most reliable for extracting QNMs. A physically motivated way to answer this question is by inspecting the stability of each mode as a function of the start time for each simulation. Specifically, we look at how the absolute values of the QNM amplitudes evolve based on a chosen fitting start time. If the amplitude of a mode is highly varying, we call this mode unstable, and therefore, we cannot fully rely on its value. To quantify this highly varying behavior, we find the variation in the mode amplitude by calculating its variance over a window of time that avoids any bias. The variance of the QNM

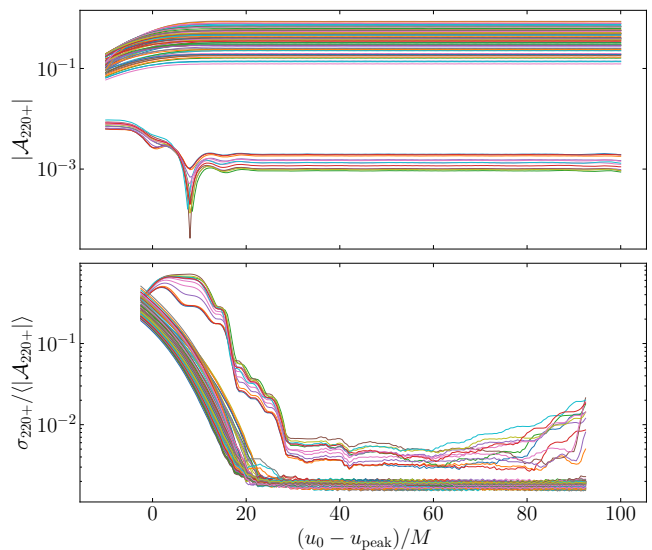


FIG. 2. The top panel shows the absolute QNM amplitudes of the $(2, 2, 0, +)$ mode as a function of the model start time u_0 for each simulation. The bottom panel shows the variance divided by the mean absolute amplitude over a time window of $15M$ for this mode amplitude.

amplitude is given by

$$\sigma_{|\mathcal{A}_{\ell mn}|}^2(u_0) = \frac{1}{\Delta u} \int_{u_0 + \Delta u/2}^{u_0 - \Delta u/2} \left(|\mathcal{A}_{\ell mn}(u)| - \langle |\mathcal{A}_{\ell mn}| \rangle \right)^2 du, \quad (2)$$

where $\langle |\mathcal{A}_{\ell mn}| \rangle$ is the average of the magnitude of the QNM amplitude over the window of time $\Delta u = 15M$. Since we are comparing fits with different choices of u_0 , we reference them all to the same fixed u_{ref} , taking out the exponential decay. For maximum stability, we choose a time within the window where the variation is at a minimum. Note that a window that is too small will have almost no variation while a large window may include values that are unphysical — leading to a high variation, as seen in the top panel of Fig. 2.

We are interested in the later times when the behavior seems to have stabilized and the modes can be reliably extracted. Note that some simulations show a smaller absolute amplitude on the order of 10^{-3} . These are the BBH systems for which the retrograde mode is dominant over the prograde mode and, therefore, the prograde mode has a smaller amplitude. To get a better idea of the $(2, 2, 0, +)$ mode stability we show in the bottom panel the variance over the mean of the absolute amplitudes over a $15M$ time window. For the $(2, 2, 0, +)$ mode, it is clear that times around and after $u_0 - u_{\text{peak}} = 20M$ are more stable and, thus, more reliable to use in our fits. If we fit for the $(2, 2, 0, -)$ mode, the curves reverse, i.e., the systems with a dominant retrograde mode have low variations after $u_0 - u_{\text{peak}} = 20M$ while the prograde-dominant systems show a jagged line. This can be seen

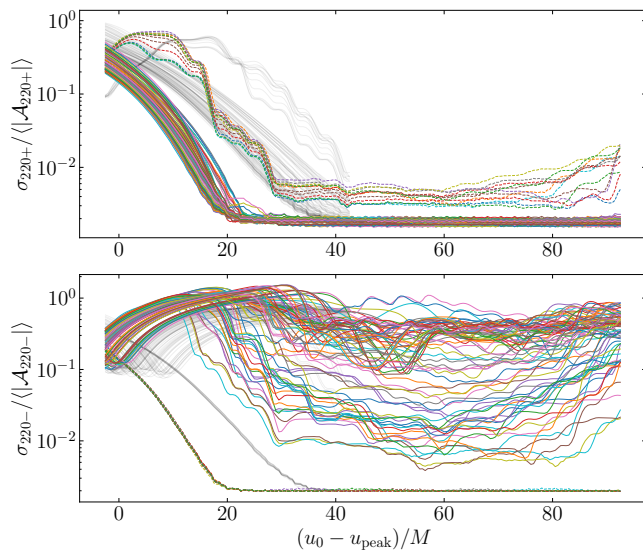


FIG. 3. The top panel shows the variance divided by the mean absolute amplitude over a $15M$ time window of the $(2, 2, 0, +)$ mode as a function of the model start time u_0 for each simulation. The bottom panel shows the corresponding quantities for the $(2, 2, 0, -)$ mode. The color lines represent the extraction of the modes when the $(2, 2, 1, \pm)$ mode is included in the fitting process while the light gray lines in the background represents the fits with only the fundamental modes are included.

by comparing the colored curves on the top and bottom panels of Fig. 3.

An important finding to note is that the variance over the mean absolute amplitude decreases when fitting the additional $(2, 2, 1, \pm)$ overtone. If we do not include the first overtone, our amplitude variances would look like the gray lines shown in Fig. 3. The top panel shows how the inclusion of the first overtone brings mode stability closer to the peak of the waveform. This tells us that including the first overtone, which can be very loud in several simulations, improves our fits. This is no surprise since similar behavior can be seen in the mismatch plots when including more than just the fundamental overtone [34]. However, one must be careful when including overtones as this can produce overfitting. Overtones higher than $n = 2$ contribute very little power at late times like $u_0 - u_{\text{peak}} = 20M$ since they decay rapidly.

As mentioned in the discussion above, the variance normalized by the mean absolute amplitude of $(2, 2, 0, -)$ is just as low in retrograde-dominated simulations as for the prograde amplitude in the prograde-dominated simulations. A striking feature of this plot is also the high variance in the retrograde mode at all times. This is the first telltale sign that fitting for these amplitudes quickly becomes challenging.

In addition to varying the fitting start time, we can use the mismatch between the NR waveform and our model at different start times to get a more physically motivated idea of which time choice to make. We define mismatch

as

$$\mathcal{M}(a, b) \equiv 1 - \text{Re} \left[\frac{\langle a, b \rangle}{\sqrt{\langle a, a \rangle \langle b, b \rangle}} \right], \quad (3)$$

where $\langle a, b \rangle$ is the inner product between waveforms a and b defined as

$$\langle a, b \rangle = \int_{S^2} \int_{u_0}^{u_f} a^*(u, \theta, \phi) b(u, \theta, \phi) du d\Omega \quad (4)$$

$$= \int_{u_0}^{u_f} \sum_{\ell, m} a_{\ell m}^*(u) b_{\ell m}(u) du \quad (5)$$

and $[u_0, u_f]$ is the interval of time for fitting the waveform with a QNM model. As seen in Fig. 4 of [14], $u_0 - u_{\text{peak}} = 20M$ is a time when the mismatch reaches a minimum but is still above numerical error. In fact, regardless of the number of modes one chooses to model, the mismatch minimum dances around $u_0 - u_{\text{peak}} = 20M$. Therefore, we choose to fit all the QNM amplitudes at this same time, i.e., the time at which we specify the QNM amplitudes is same for all QNMs.

IV. BUILDING THE SURROGATE

There are various ways to approach building a ringdown surrogate. In this work, we do not need to directly model the waveforms' time dependence for all of the parameter space but instead, we build a map from BBH system parameters like initial masses and spins to the remnant parameters of mass, spin, and complex-valued QNM mode amplitudes. That is, we use all of the BBH system data and make predictions for systems with parameters that have not been simulated.

The surrogate model is implemented using Gaussian process regression, which provides us with a sophisticated mathematical tool to find joint Gaussian distributions between the system data and the predictions [35]. This method allows us to interpolate between data sets and estimate the errors of the fitted quantities. More specifically, we are using the GPR fitting method employed in [10], which is built using `scikit-learn` [36].

In the rest of this section, we discuss the choice of modes included in the ringdown surrogate model. We also show the preparation needed to curate a dataset for GPR as well as the methods used for training and testing the dataset.

A. Modes Modelled

Based on the analyses performed in Sec. III, we can confidently include 10 QNM amplitudes in this ringdown surrogate model: $(2, 2, 0, +)$, $(2, -2, 0, -)$, $(2, 2, 1, +)$, $(2, -2, 1, -)$, $(2, 0, 0, \pm)$, $(3, 2, 0, +)$, $(3, -2, 0, -)$, $(4, 4, 0, +)$, and $(4, -4, 0, -)$. Notably, due to the large

variance of the retrograde modes across simulations (see Fig. 3), our surrogate model does not include them as the resulting GPR fits were inaccurate. As we have seen from Fig. 1, this affects a corner of parameter space with a high mass ratio and highly negative effective spin,

$$\chi_{\text{eff}} = \frac{q\chi_1 + \chi_2}{1 + q} = \frac{m_1\chi_1 + m_2\chi_2}{m_1 + m_2}. \quad (6)$$

One possible remedy may be to increase the weight that GPR gives to the retrograde modes for these simulations. Another possible option would be to “zero out” the amplitude values that are not dominant, such that the prograde(retrograde) mode would be non-zero for simulations where the prograde(retrograde) is dominant over the retrograde(prograde). The downside to this solution is that we may miss out on important physics. In future work, we will be investigating the best way to include retrograde modes.

A second noticeable aspect of the surrogate model is that we do not take into account the $(2, \pm 1, 0, +)$ and $(3, \pm 3, 0, +)$ modes. Not very surprisingly, it turns out that the QNM amplitudes for these modes are very small when looking at BBH systems with a mass ratio of one. The inherent symmetries of equal mass systems cause multipoles with an odd m number to be zero. Since many of the simulations have a mass ratio of one or close to one, GPR is not able to predict as smoothly across parameter space. One can in principle include the modes in the model, but their trustworthiness would be questionable. As of now, we do not have a clear way to remedy this challenge, but it is something we will be working toward shortly as we improve the robustness of the surrogate model.

B. Numerical Relativity Waveforms and Dataset

For this surrogate model, we use 102 binary black hole mergers evolved by the SXS Spectral Einstein Code (SpEC) [37]. These are the same systems used to create NRHybSur3dq8 and NRHybSur3dq8_CCE [13, 19]. The waveforms are extracted using Cauchy-characteristic evolution (CCE) from SpECTRE and a BMS transformation is applied to them. In this way, they are supertranslated so that the remnant black hole is in the superrest frame [18, 38–42]. The mass ratios spanned by this set of simulations are in the range $q \leq 8$ with the primary and secondary spins ranging as $\chi_z^{1,2} \in [-0.8, 0.8]$, as shown in Fig. 1. The initial parameters of these simulations are specified at a reference time after the effects of junk radiation have sufficiently decayed [43].

The dataset consists of initial BBH and remnant parameters for each BBH system. The initial parameters we use are $\{\log(q), \hat{\chi}, \chi_a\}$, where $\hat{\chi}$ is the spin parameter that enters the GW phase at leading order [44–47] in the post-Newtonian expression and is defined as

$$\hat{\chi} = \frac{\chi_{\text{eff}} - 38\eta(\chi_{1z} + \chi_{2z})/113}{1 - 76\eta/113}, \quad (7)$$

and χ_a is the anti-symmetric spin given by

$$\chi_a = \frac{1}{2}(\chi_{1z} - \chi_{2z}). \quad (8)$$

Just as in [10], we found this parametrization gives more accurate predictions than using $\{q, \chi_{1z}, \chi_{2z}\}$. We obtain the remnant mass and spin from \mathcal{S}^+ by using Poincaré charges rather than the apparent horizon [48].

As done in Sec. III A, we begin preparing our dataset by first aligning the waveforms so that the peak of the L^2 norm is at $u_0 - u_{\text{peak}} = 0M$. As before we fix the $U(1)$ rotational symmetry of the systems so that the $(2, 2)$ spherical mode is real and positive at $u_0 - u_{\text{peak}} = 20M$. Once we have rotated our waveforms, we are ready to use them in the QNM fitting algorithm [49]. Fitting for the QNMs at $u_0 - u_{\text{peak}} = 20M$ gives us the QNM amplitude values that we will be using in our training and testing dataset. Since `scikit-learn`’s GPR does not take complex values, we decompose our complex QNM amplitudes into real and imaginary parts. Therefore, we model $\{m_f, \chi_f, \Re[\mathcal{A}_{\ell mn}], \Im[\mathcal{A}_{\ell mn}]\}$ as a function of $(\log(q), \hat{\chi}, \chi_a)$. For example, our remnant mass model is given by $m_f(\log(q), \hat{\chi}, \chi_a)$. Machine learning (ML) algorithms require the data to be standardized, i.e., have a zero mean and unit variance. We pre-process the data before training the algorithm as in [10], i.e., we subtract a linear fit and the mean from the data points and then normalize them. When evaluating the fits, the inverse transformations are applied.

Before analyzing the results, we need to calculate the numerical error in our waveforms. We perform this calculation by taking the highest and second-highest resolution waveforms such that the error between them is given by

$$\mathcal{E}[a, b] \equiv \frac{1}{2} \frac{\langle a - b | a - b \rangle}{\langle a | a \rangle}, \quad (9)$$

where a represents the highest resolution NR waveform available and b is the second highest resolution waveform. This equation was first introduced in [50] as related to the weighted average of the all-mode mismatch.

C. Training and Testing

The most common way to train any ML algorithm is to separate the dataset into two parts: training and testing. Often, 70% of a dataset is used in training and 30% for testing. However, this is usually for datasets that contain tens of thousands of data points or more. For small datasets like ours, this is a problem since only a fraction of the data would be used in training. To mitigate this problem, we instead employ k -fold cross-validation. This method entails equally dividing a dataset into k smaller subsets, using one of these subsets for predicting and taking the remaining $k - 1$ for training. This is then repeated k times until each subset is used for validation. For large datasets, this could present a problem since one

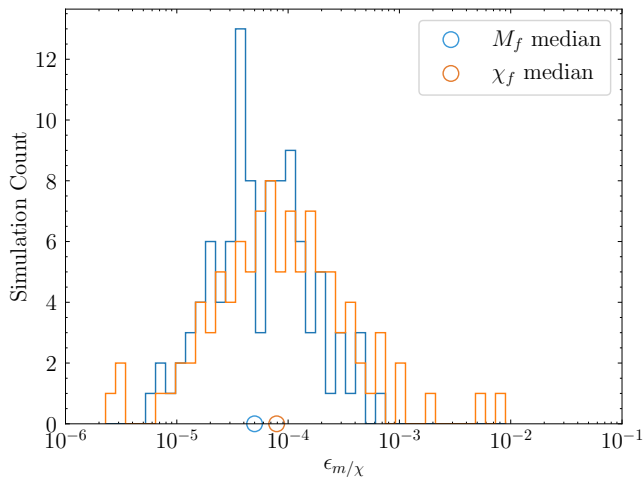


FIG. 4. A histogram showing the relative error in remnant mass (blue) and the absolute difference in the remnant spin (orange) as calculated in Eqs. (10) and (11), respectively. The median errors are denoted by the circles on the horizontal axis.

must train k models instead of one. However, our dataset is small enough that the additional training time does not outweigh the benefits of the method. We use a value of $k = 20$, where all datasets contain 5 simulations except for three of them which contain 6 since the number of simulations is not divisible by 5. This way of splitting the dataset allows us to train and test over our entire dataset. Additionally, k -fold cross-validation gives us errors for each k -fold we test. Since we use a value of $k = 20$, we get 20 values of testing errors, which we average and use as an estimation of the model's error.

V. RESULTS

Running GPR with the settings discussed above, we get predictions for each k -fold testing dataset. Figure 4 shows how well the surrogate model does in recovering the remnant mass and spin. The error in the remnant mass is the relative error defined as

$$\epsilon_m = \frac{|m_f^{\text{NR}} - m_f^{\text{Surr}}|}{m_f^{\text{NR}}}, \quad (10)$$

while the error in spin is the absolute difference given by

$$\epsilon_\chi = |\chi_f^{\text{NR}} - \chi_f^{\text{Surr}}|. \quad (11)$$

Note that both errors are low and agree with the results from the remnant surrogate of [10]. The median error in the remnant mass is 5×10^{-5} while the median error in the remnant spin is $\sim 8 \times 10^{-5}$. The 95th percentile errors are 3.2×10^{-3} and 6.8×10^{-4} , respectively.

For errors in predicting the QNM amplitudes, we cal-

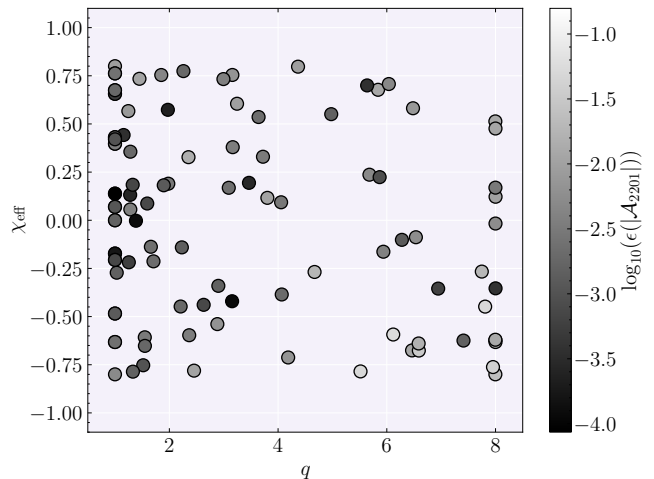


FIG. 5. The relative errors of the magnitude of the $(2, 2, 0, +)$ mode amplitude across parameter space.

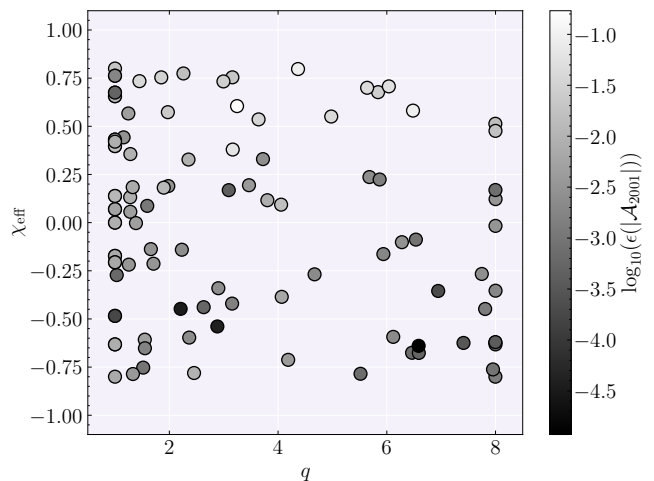


FIG. 6. The relative errors of the magnitude of the $(2, 0, 0, +)$ mode amplitude across parameter space.

culate the relative errors,

$$\epsilon(|\mathcal{A}_{\ell mn}|) = \frac{||\mathcal{A}_{\ell mn}^{\text{QNM}}| - |\mathcal{A}_{\ell mn}^{\text{Surr}}||}{|\mathcal{A}_{\ell mn}^{\text{QNM}}|}, \quad (12)$$

of the magnitude $|\mathcal{A}_{\ell mn}|$ over parameter space. Here $\mathcal{A}_{\ell mn}^{\text{QNM}}$ denotes the complex-valued QNM amplitudes extracted from the NR data while $\mathcal{A}_{\ell mn}^{\text{Surr}}$ denotes the surrogate model of $\mathcal{A}_{\ell mn}^{\text{QNM}}$. Fig. 5 illustrates the error in predicting the $(2, 2, 0, +)$ mode amplitude over parameter space. Furthermore, we show the errors for the $(2, 0, 0, +)$ and $(4, 4, 0, +)$ modes in Figs. 6 and 7. Overall, the median values for the amplitude errors are listed in Table I. Although the table only lists the $+m$ prograde modes, the relative errors for the $-m$ prograde modes are the same due to mode symmetries in spin-aligned systems. The first two error columns show the values for the relative

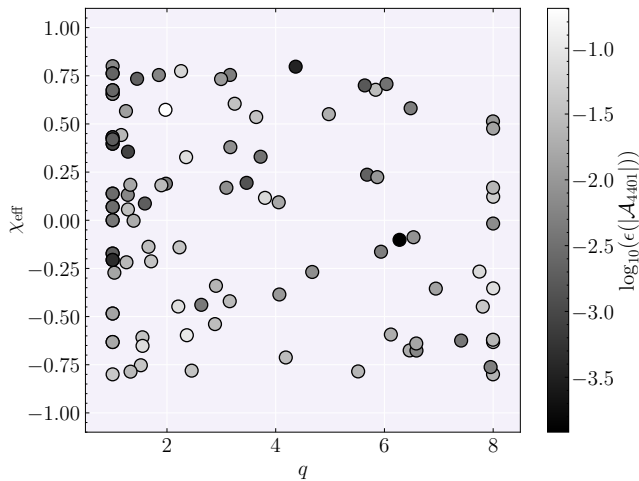


FIG. 7. The relative errors of the magnitude of the $(4, 4, 0, +)$ mode amplitude across parameter space.

QNM	$\epsilon(\Re[\mathcal{A}_{\ell mn}])$	$\epsilon(\Im[\mathcal{A}_{\ell mn}])$	$\epsilon(\mathcal{A}_{\ell mn})$
$(2, 2, 0, +)$	0.0020	0.061	0.0024
$(2, 2, 1, +)$	0.060	0.064	0.050
$(2, 0, 0, +)$	0.0026	0.0089	0.0037
$(3, 2, 0, +)$	0.024	0.012	0.0084
$(4, 4, 0, +)$	0.035	0.011	0.011

TABLE I. Table showing the median relative errors of the real, imaginary, and absolute QNM amplitudes predicted. The relative errors for each simulation are defined in Eqs. (12) and (13).

amplitude errors for the real and imaginary components, calculated as

$$\epsilon(\Re[\mathcal{A}_{\ell mn}]) = \left| \frac{\Re[\mathcal{A}_{\ell mn}^{\text{QNM}}] - \Re[\mathcal{A}_{\ell mn}^{\text{SURR}}]}{\Re[\mathcal{A}_{\ell mn}^{\text{QNM}}]} \right|. \quad (13)$$

For the last column, we combine the real and imaginary components to get the complex QNM amplitude and calculate the relative error of the absolute amplitudes using Eq. (12). Unsurprisingly, the absolute amplitude errors are smallest for the $(2, 2, 0, +)$ and $(2, -2, 0, -)$ modes which are always the dominant modes in these simulations. Nevertheless, one can see that even modes with smaller magnitudes are well recovered.

In Fig. 8 we show the mismatches between the different types of waveforms for all the simulations. The calculation of the mismatches includes only the QNMs in the surrogate and is not for the true all-mode mismatches. The blue histogram shows the mismatch distribution between NR and the surrogate waveform. The median value is of 1.6×10^{-4} and can be seen in blue on the horizontal axis. The orange histogram shows the mismatch distribution between the QNM model and the surrogate model. As expected, the median mismatch, shown in orange, is lower at 1.7×10^{-5} . We also include the median values for the mismatches between NR and the QNM model in black,

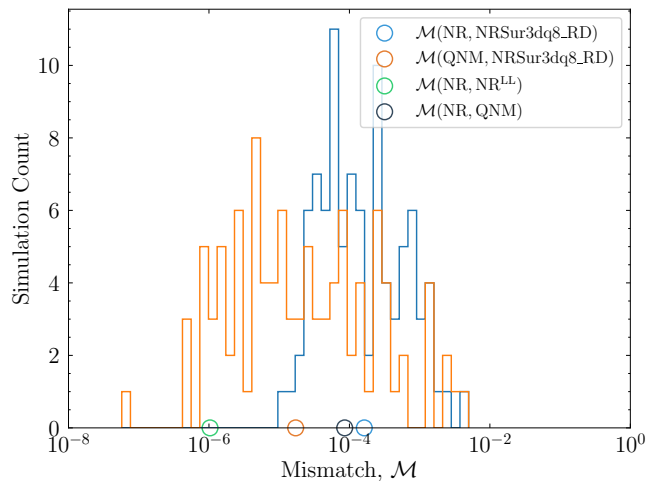


FIG. 8. The mismatch distribution of simulations. The blue histogram shows the mismatch between the NR waveforms and surrogate model, while the orange histogram shows the mismatch between the QNM and surrogate models. The green circle on the horizontal axis highlights the median numerical error with the label “LL” for “Lower Lev”, i.e., the next-highest resolution simulation. The median mismatch between NR and the QNM model is shown with the black circle.

which is just slightly lower than that of the surrogate model, and the mismatch from the numerical waveform resolutions in green. The mismatch in the highest and the next-highest waveform resolutions is around 1×10^{-6} , as calculated from Eq. 9. Since our model mismatches are higher than those coming from numerical error, we do not expect any overfitting.

Finally, Figs. 9 and 10 show how these predicted mode amplitudes translate to the waveform strain. In both plots, the top panel shows the real part of the $\ell = m = 2$ NR waveform strain (black), the QNM model (blue), and the surrogate model (orange) for two different systems. Both the QNM model and the surrogate model include the $(2, 2, 0, +)$ and $(2, 2, 1, +)$ modes. In Fig. 9, we take the waveform that has the largest mismatch between NR and our QNM model while in Fig. 10 we choose the NR waveform with the smallest mismatch.

In the bottom panels of both figures, we show the residuals between NR and the surrogate model. Focusing on the black line on Fig. 9, we see that at $u - u_{\text{peak}} = 20M$ the residual is on the order of 10^{-3} . This is the worst-case scenario we expect to predict within the training region. Not surprisingly, the waveform with the worst mismatch corresponds to a simulation with a mass ratio of $q = 8$ and spins of $\chi = -0.8$. This is the area of parameter space that showed a preference for the retrograde mode amplitudes (which is neglected in our both our QNM and surrogate models), and therefore, the $(2, 2)$ mismatch is higher. On the other extreme, Fig. 10 shows a residual of 10^{-4} . We also show 10^{-3} order of magnitude residuals of the surrogate model for the $(2, 0, 0, \pm)$ and $(4, 4, 0, +)$ modes in Figs. 11 and 12, respectively. From Figs. 9, 11,

and 12 one can visually see the differences between the NR waveform and `NRSur3dq8_RD`. This highlights the importance of using more than just the (2, 2) for modeling a BBH system [31, 34, 51–57].

In Fig. 13, we show the full modelling power of the surrogate model by using the NR waveform containing only the modes modelled by the surrogate overlaid with the strain from the QNM and surrogate models. To get the full waveforms, we take the strain of each mode modelled at all times and multiply by the corresponding spherical harmonics at chosen angles ($\theta = \pi/3, \phi = \pi/4$). Note that the strains on the top panel are indistinguishable from each other by eye. However, the bottom panel shows the residuals between the NR waveform and our surrogate are $\sim 1 \times 10^{-3}$ for a QNM fitting start time of $20M$ after peak.

VI. CONCLUSION

We have introduced the first ringdown surrogate model `NRSur3dq8_RD` that uses CCE waveforms, i.e., waveforms with memory effects, in the superrest frame of the remnant. Using waveforms that have been mapped to the same BMS frame as that of the QNM model is crucial in performing ringdown analyses since this is implicitly assumed for QNM solutions of the Teukolsky equation [1]. This BMS frame fixing causes the strain to not only be shifted by a constant but also introduces mode-mixing, as seen in Figs. 6–8 of [14]. Therefore, we fit for the QNM amplitudes with these CCE waveforms. Using the same fitting methods from [14], we build a GPR algorithm that allows us to extract the remnant mass, remnant spin, and a set of 10 QNM amplitudes. The median errors in mass and spin are 10^{-5} , while our prediction errors for the complex-valued QNM amplitudes, shown in Table I, are typically 10^{-2} to 10^{-3} . These results highlight the high fidelity of our surrogate model for extracting high-order modes. For a visual of the ringdown model, Figs. 9–13 show the good correspondence between the NR waveform and the surrogate model. These figures also show an example of the small residuals between NR and surrogate waveforms.

There are a few improvements to this ringdown surrogate model that we plan to implement next. Apart from overcoming the challenges with the predictions of retrograde and odd- m QNMs (discussed in Sec. IV A), we plan to include mode amplitudes coming from second-order perturbation theory since recent works have shown their importance in precision modelling [58, 59]. Additionally, we plan to model more general systems that may include precession. This would require us to fit for the spin orientation and not just the spin magnitude. This new model is publicly available through the python package `surfinBH` and will continue being updated with the improvements mentioned above. With these tools in hand, we will be more prepared to face gravitational-wave detections with a rich QNM spectrum.

Moreover, a recent study has taken a different approach

to predicting the QNMs by finding an analytical fit for the amplitude and phase of each complex mode [60]. Using SXS extrapolated waveforms, they can recover amplitudes for the (2, 2, 0, 1) and (2, 2, 1, 1) modes with errors on par with our results. However, for higher harmonics, the fitting formula shows amplitude errors that are almost an order of magnitude higher than the results from Table I, making it difficult to extract these QNMs.

Note added.—While preparing this article, we learned that Pacilio et al. have built a surrogate model similar to ours [61]. We plan to validate our models against each other in the future.

ACKNOWLEDGMENTS

The authors would like to thank Tousif Islam, Costantino Pacilio, Swetha Bhagwat, Francesco Nobili, and Davide Gerosa for helpful discussions. Some calculations were performed with the Wheeler cluster at the California Institute of Technology (Caltech), which is supported by the Sherman Fairchild Foundation and by Caltech.

The work of L.M.Z. was partially supported by the MSSGC Graduate Research Fellowship, awarded through the NASA Cooperative Agreement 80NSSC20M0101. L.C.S. was supported by NSF CAREER Award PHY-2047382 and a Sloan Foundation Research Fellowship. K.M. was supported by the Sherman Fairchild Foundation and NSF Grants No. PHY-2011968, PHY-2011961, PHY-2309211, PHY-2309231, and OAC-2209656 at Caltech. S.E.F. was supported by NSF Grant No. PHY-2110496. V.V. was supported by NSF Grant No. PHY-2309301. S.E.F. and V.V. were supported by UMass Dartmouth’s Marine and Undersea Technology (MUST) research program funded by the Office of Naval Research (ONR) under grant no. N00014-23-1-2141.

REFERENCES

- [1] S. A. Teukolsky, Perturbations of a Rotating Black Hole. I. Fundamental Equations for Gravitational, Electromagnetic, and Neutrino-Field Perturbations, *Astrophys. J.* **185**, 635 (1973).
- [2] S. L. Detweiler, Black Holes and Gravitational Waves. III. The Resonant Frequencies of Rotating Holes, *Astrophys. J.* **239**, 292 (1980).
- [3] E. W. Leaver, An Analytic representation for the quasi normal modes of Kerr black holes, *Proc. Roy. Soc. Lond. A* **402**, 285 (1985).
- [4] S. R. Dolan and A. C. Ottewill, On an Expansion Method for Black Hole Quasinormal Modes and Regge Poles, *Class. Quant. Grav.* **26**, 225003 (2009), [arXiv:0908.0329 \[gr-qc\]](https://arxiv.org/abs/0908.0329).
- [5] A. Buonanno and T. Damour, Effective one-body approach to general relativistic two-body dynamics, *Phys. Rev. D* **59**, 084006 (1999), [arXiv:gr-qc/9811091](https://arxiv.org/abs/gr-qc/9811091).
- [6] A. Albertini, A. Nagar, P. Rettegno, S. Albanesi, and R. Gamba, Waveforms and fluxes: Towards a self-consistent effective one body waveform model for non-

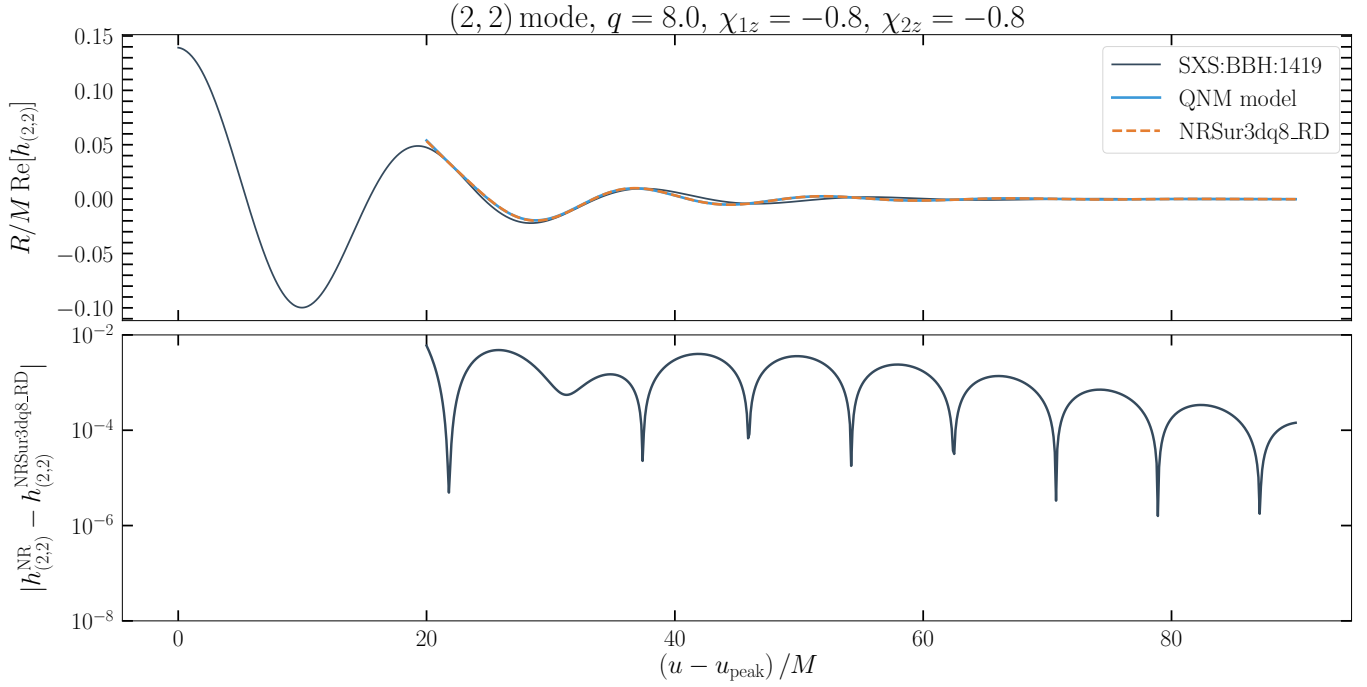


FIG. 9. We plot the worst performance, or greatest mismatch, between the real component of the (2, 2) mode of a CCE waveform, the best-fit QNM model built from the (2, 2) mode with $n = 0$ and the first overtone, and the surrogate. The upper panel shows NR waveform SXS:BBH:1419 (black), the QNM model (blue), and NRSur3dq8_RD (orange). The lower panels show the residuals between NR and NRSur3dq8_RD waveforms.

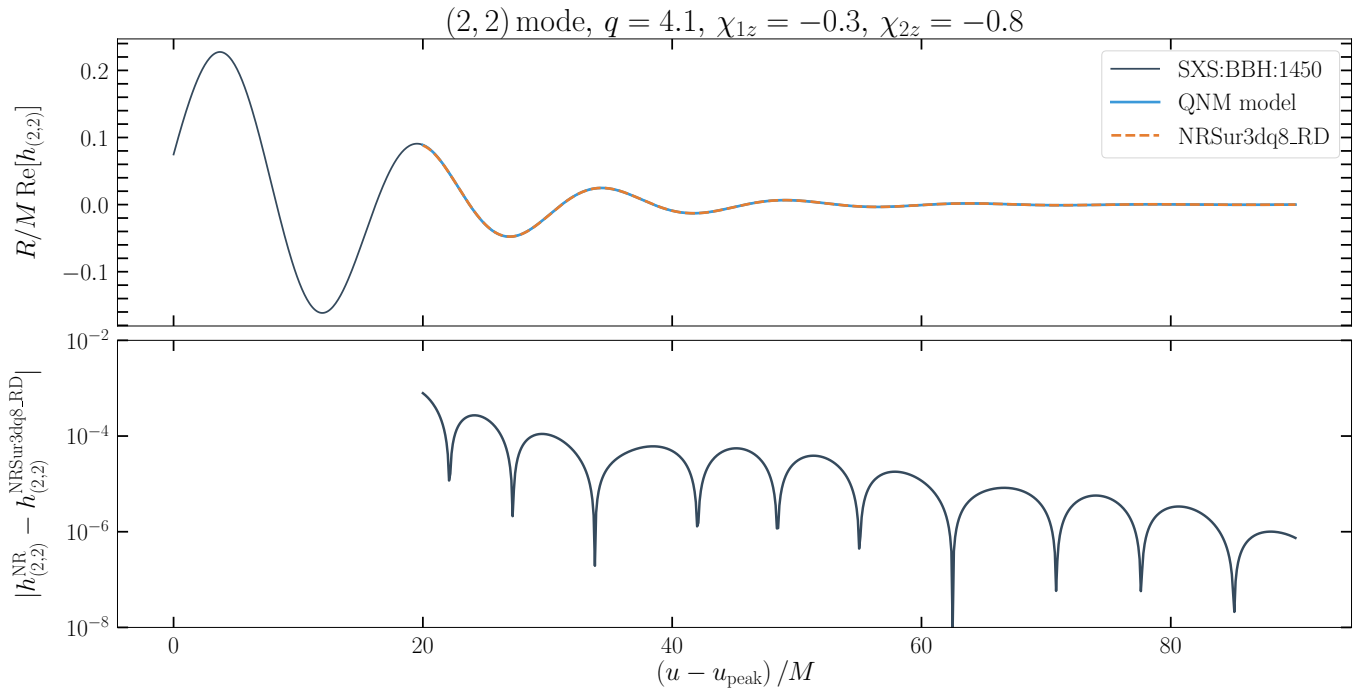


FIG. 10. Similar to Fig. 9, but the case with smallest mismatch between NR waveform SXS:BBH:1450 and the surrogate.

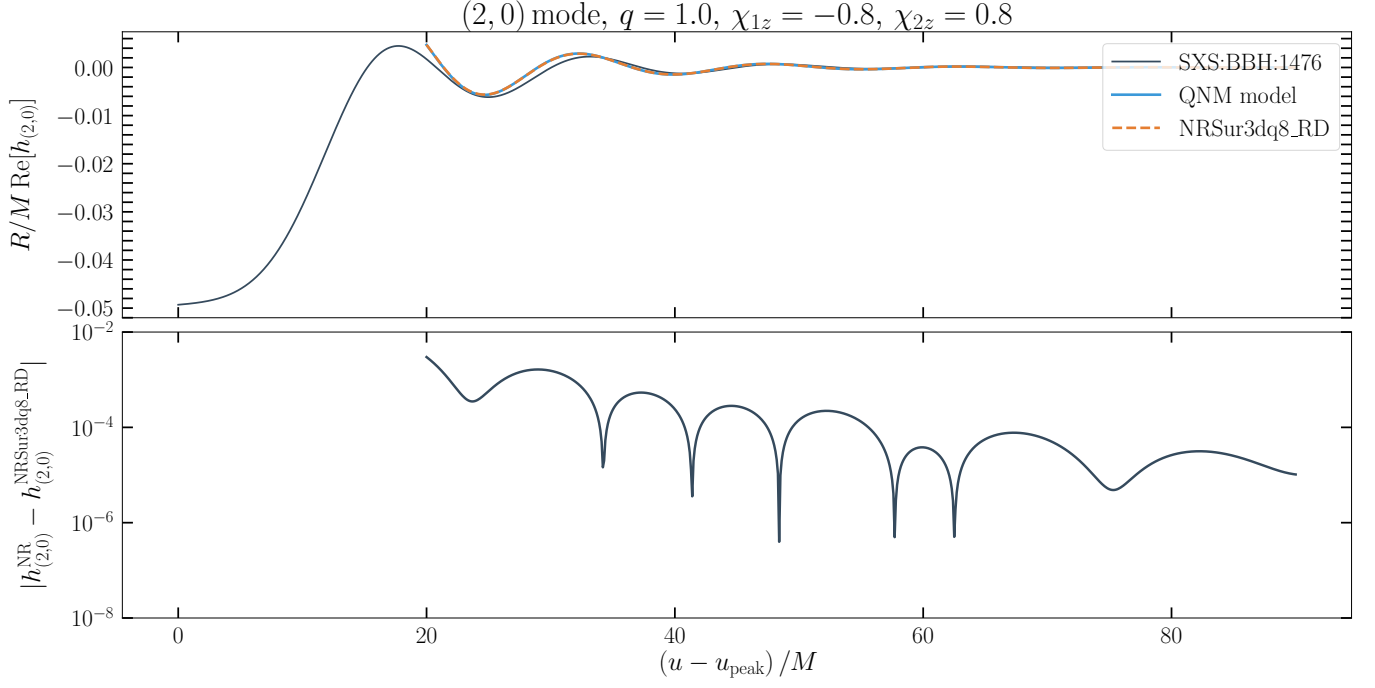


FIG. 11. Similar to Fig. 9, but the case with median mismatch between NR waveform SXS:BBH:1476 and the surrogate, showing the (2, 0) mode and the reconstruction using both prograde and retrograde modes (2, 0, 0, \pm).

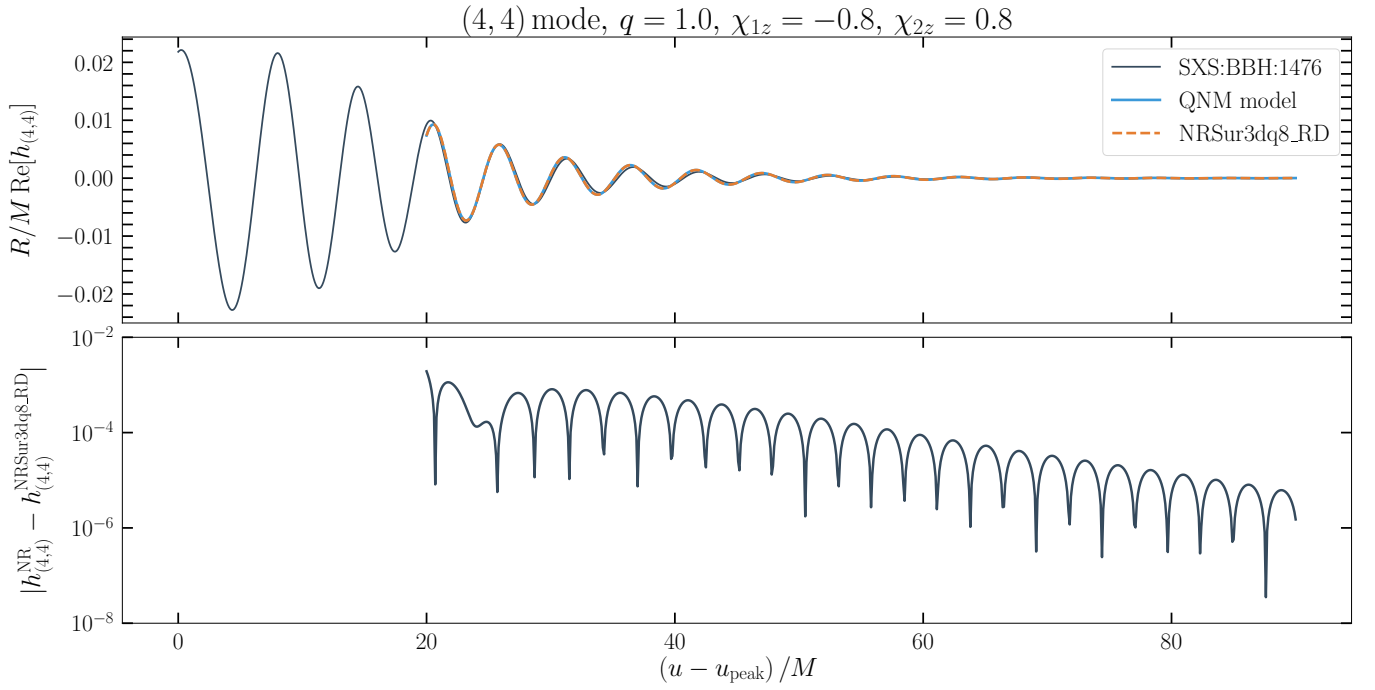


FIG. 12. Same NR waveform as Fig. 11, but showing the real component of the (4, 4) mode using the fundamental mode.

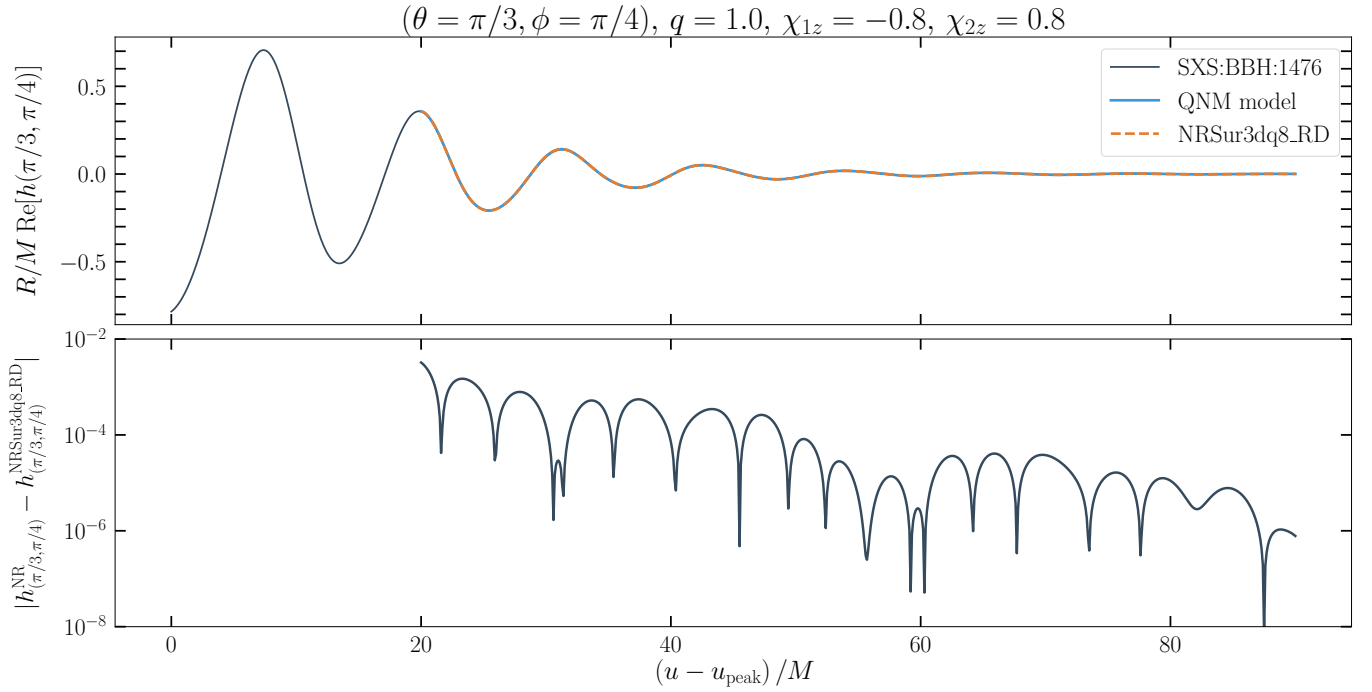


FIG. 13. Same NR waveform as Fig. 11. The real component of the strain measured by an observer at $(\theta = \pi/3, \phi = \pi/4)$. The strain is reconstructed from all harmonics used in NRSur3dq8_RD.

- precessing, coalescing black-hole binaries for third generation detectors, *Phys. Rev. D* **105**, 084025 (2022), [arXiv:2111.14149 \[gr-qc\]](#).
- [7] M. Pürrer and C.-J. Haster, Gravitational waveform accuracy requirements for future ground-based detectors, *Phys. Rev. Res.* **2**, 023151 (2020), [arXiv:1912.10055 \[gr-qc\]](#).
- [8] H. Estellés *et al.*, A Detailed Analysis of GW190521 with Phenomenological Waveform Models, *Astrophys. J.* **924**, 79 (2022), [arXiv:2105.06360 \[gr-qc\]](#).
- [9] S. E. Field, C. R. Galley, J. S. Hesthaven, J. Kaye, and M. Tiglio, Fast prediction and evaluation of gravitational waveforms using surrogate models, *Phys. Rev. X* **4**, 031006 (2014), [arXiv:1308.3565 \[gr-qc\]](#).
- [10] V. Varma, D. Gerosa, L. C. Stein, F. Hébert, and H. Zhang, High-accuracy mass, spin, and recoil predictions of generic black-hole merger remnants, *Phys. Rev. Lett.* **122**, 011101 (2019), [arXiv:1809.09125 \[gr-qc\]](#).
- [11] T. Islam, S. E. Field, S. A. Hughes, G. Khanna, V. Varma, M. Giesler, M. A. Scheel, L. E. Kidder, and H. P. Pfeiffer, Surrogate model for gravitational wave signals from nonspinning, comparable-to large-mass-ratio black hole binaries built on black hole perturbation theory waveforms calibrated to numerical relativity, *Phys. Rev. D* **106**, 104025 (2022), [arXiv:2204.01972 \[gr-qc\]](#).
- [12] M. Walker, V. Varma, G. Lovelace, and M. A. Scheel, Numerical-relativity surrogate modeling with nearly extremal black-hole spins, *Class. Quant. Grav.* **40**, 055003 (2023), [arXiv:2208.02927 \[gr-qc\]](#).
- [13] V. Varma, S. E. Field, M. A. Scheel, J. Blackman, L. E. Kidder, and H. P. Pfeiffer, Surrogate model of hybridized numerical relativity binary black hole waveforms, *Phys. Rev. D* **99**, 064045 (2019), [arXiv:1812.07865 \[gr-qc\]](#).
- [14] L. Magaña Zertuche *et al.*, High precision ringdown modeling: Multimode fits and BMS frames, *Phys. Rev. D* **105**, 104015 (2022), [arXiv:2110.15922 \[gr-qc\]](#).
- [15] H. Bondi, M. G. J. Van der Burg, and A. W. K. Metzner, Gravitational waves in general relativity, VII. Waves from axi-symmetric isolated system, *Proceedings of the Royal Society of London. Series A. Mathematical and Physical Sciences* **269**, 21 (1962).
- [16] R. K. Sachs and H. Bondi, Gravitational waves in general relativity VIII. Waves in asymptotically flat space-time, *Proceedings of the Royal Society of London. Series A. Mathematical and Physical Sciences* **270**, 103 (1962).
- [17] M. Boyle, Transformations of asymptotic gravitational-wave data, *Phys. Rev. D* **93**, 084031 (2016), [arXiv:1509.00862 \[gr-qc\]](#).
- [18] K. Mitman *et al.*, Fixing the BMS frame of numerical relativity waveforms, *Phys. Rev. D* **104**, 024051 (2021), [arXiv:2105.02300 \[gr-qc\]](#).
- [19] J. Yoo *et al.*, Numerical relativity surrogate model with memory effects and post-Newtonian hybridization, *Phys. Rev. D* **108**, 064027 (2023), [arXiv:2306.03148 \[gr-qc\]](#).
- [20] R. Abbott *et al.* (LIGO Scientific, Virgo), GW190521: A Binary Black Hole Merger with a Total Mass of $150M_{\odot}$, *Phys. Rev. Lett.* **125**, 101102 (2020), [arXiv:2009.01075 \[gr-qc\]](#).
- [21] B. Sathyaprakash *et al.*, Scientific Objectives of Einstein Telescope, *Class. Quant. Grav.* **29**, 124013 (2012), [Erratum: *Class. Quant. Grav.* **30**, 079501 (2013)], [arXiv:1206.0331 \[gr-qc\]](#).
- [22] B. P. Abbott *et al.* (LIGO Scientific), Exploring the Sensitivity of Next Generation Gravitational Wave Detectors, *Class. Quant. Grav.* **34**, 044001 (2017), [arXiv:1607.08697 \[astro-ph.IM\]](#).
- [23] J. Bellovary *et al.* (NASA LISA Study Team), Getting

- Ready for LISA: The Data, Support and Preparation Needed to Maximize US Participation in Space-Based Gravitational Wave Science, (2020), [arXiv:2012.02650 \[astro-ph.IM\]](#).
- [24] V. Kalogera *et al.*, The Next Generation Global Gravitational Wave Observatory: The Science Book, (2021), [arXiv:2111.06990 \[gr-qc\]](#).
- [25] V. Baibhav, E. Berti, D. Gerosa, M. Mapelli, N. Giacobbo, Y. Bouffanais, and U. N. Di Carlo, Gravitational-wave detection rates for compact binaries formed in isolation: LIGO/Virgo O3 and beyond, *Phys. Rev. D* **100**, 064060 (2019), [arXiv:1906.04197 \[gr-qc\]](#).
- [26] V. Varma, L. C. Stein, and D. Gerosa, [vijayvarma392/surfinBH: Surrogate Final BH properties](#) (2018).
- [27] W. H. Press and S. A. Teukolsky, Perturbations of a Rotating Black Hole. II. Dynamical Stability of the Kerr Metric, *Astrophys. J.* **185**, 649 (1973).
- [28] L. London and E. Fauchon-Jones, On modeling for Kerr black holes: Basis learning, QNM frequencies, and spherical-spheroidal mixing coefficients, *Class. Quant. Grav.* **36**, 235015 (2019), [arXiv:1810.03550 \[gr-qc\]](#).
- [29] H. Lim, G. Khanna, A. Apte, and S. A. Hughes, Exciting black hole modes via misaligned coalescences: II. The mode content of late-time coalescence waveforms, *Phys. Rev. D* **100**, 084032 (2019), [arXiv:1901.05902 \[gr-qc\]](#).
- [30] M. Isi and W. M. Farr, Analyzing black-hole ringdowns, (2021), [arXiv:2107.05609 \[gr-qc\]](#).
- [31] X. Li, L. Sun, R. K. L. Lo, E. Payne, and Y. Chen, Angular emission patterns of remnant black holes, *Phys. Rev. D* **105**, 024016 (2022), [arXiv:2110.03116 \[gr-qc\]](#).
- [32] G. B. Cook and M. Zalutskiy, Gravitational perturbations of the Kerr geometry: High-accuracy study, *Phys. Rev. D* **90**, 124021 (2014), [arXiv:1410.7698 \[gr-qc\]](#).
- [33] L. C. Stein, qnm: A Python package for calculating Kerr quasinormal modes, separation constants, and spherical-spheroidal mixing coefficients, *J. Open Source Softw.* **4**, 1683 (2019), [arXiv:1908.10377 \[gr-qc\]](#).
- [34] M. Giesler, M. Isi, M. A. Scheel, and S. Teukolsky, Black Hole Ringdown: The Importance of Overtones, *Phys. Rev. X* **9**, 041060 (2019), [arXiv:1903.08284 \[gr-qc\]](#).
- [35] C. Rasmussen and C. Williams, *Gaussian Processes for Machine Learning* (MIT Press, 2006).
- [36] F. Pedregosa, G. Varoquaux, A. Gramfort, V. Michel, B. Thirion, O. Grisel, M. Blondel, P. Prettenhofer, R. Weiss, V. Dubourg, J. VanderPlas, A. Passos, D. Cournapeau, M. Brucher, M. Perrot, and E. Duchesnay, Scikit-learn: Machine learning in python, *CoRR abs/1201.0490* (2012), 1201.0490.
- [37] SpECCode, <https://www.black-holes.org/code/SpEC.html>.
- [38] J. Moxon, M. A. Scheel, and S. A. Teukolsky, Improved Cauchy-characteristic evolution system for high-precision numerical relativity waveforms, *Phys. Rev. D* **102**, 044052 (2020), [arXiv:2007.01339 \[gr-qc\]](#).
- [39] J. Moxon, M. A. Scheel, S. A. Teukolsky, N. Deppe, N. Fischer, F. Hébert, L. E. Kidder, and W. Throwe, The SpECTRE Cauchy-characteristic evolution system for rapid, precise waveform extraction, (2021), [arXiv:2110.08635 \[gr-qc\]](#).
- [40] N. Deppe, W. Throwe, L. E. Kidder, N. L. Vu, F. Hébert, J. Moxon, C. Armaza, G. S. Bonilla, Y. Kim, P. Kumar, G. Lovelace, A. Macedo, K. C. Nelli, E. O’Shea, H. P. Pfeiffer, M. A. Scheel, S. A. Teukolsky, N. A. Wittek, I. Anantpurkar, M. Boyle, A. Carpenter, A. Ceja, H. Chaudhary, F. Foucart, N. Ghadiri, M. Giesler, J. S. Guo, D. A. B. Iozzo, I. Legred, D. Li, S. Ma, D. Melchor, M. Morales, E. R. Most, M. A. Pajkos, T. Ramirez, L. C. Stein, S. Thomas, D. Vieira, T. Wlodarczyk, and D. Wu, [SpECTRE](#) (2024).
- [41] K. Mitman, J. Moxon, M. A. Scheel, S. A. Teukolsky, M. Boyle, N. Deppe, L. E. Kidder, and W. Throwe, Computation of displacement and spin gravitational memory in numerical relativity, *Phys. Rev. D* **102**, 104007 (2020), [arXiv:2007.11562 \[gr-qc\]](#).
- [42] K. Mitman *et al.*, Adding gravitational memory to waveform catalogs using BMS balance laws, *Phys. Rev. D* **103**, 024031 (2021), [arXiv:2011.01309 \[gr-qc\]](#).
- [43] M. Boyle *et al.*, The SXS Collaboration catalog of binary black hole simulations, *Class. Quant. Grav.* **36**, 195006 (2019), [arXiv:1904.04831 \[gr-qc\]](#).
- [44] S. Khan, S. Husa, M. Hannam, F. Ohme, M. Pürrer, X. Jiménez Forteza, and A. Bohé, Frequency-domain gravitational waves from nonprecessing black-hole binaries. II. A phenomenological model for the advanced detector era, *Phys. Rev. D* **93**, 044007 (2016), [arXiv:1508.07253 \[gr-qc\]](#).
- [45] P. Ajith, Addressing the spin question in gravitational-wave searches: Waveform templates for inspiralling compact binaries with nonprecessing spins, *Phys. Rev. D* **84**, 084037 (2011), [arXiv:1107.1267 \[gr-qc\]](#).
- [46] C. Cutler and E. E. Flanagan, Gravitational waves from merging compact binaries: How accurately can one extract the binary’s parameters from the inspiral wave form?, *Phys. Rev. D* **49**, 2658 (1994), [arXiv:gr-qc/9402014](#).
- [47] E. Poisson and C. M. Will, Gravitational waves from inspiraling compact binaries: Parameter estimation using second postNewtonian wave forms, *Phys. Rev. D* **52**, 848 (1995), [arXiv:gr-qc/9502040](#).
- [48] D. A. B. Iozzo *et al.*, Comparing Remnant Properties from Horizon Data and Asymptotic Data in Numerical Relativity, *Phys. Rev. D* **103**, 124029 (2021), [arXiv:2104.07052 \[gr-qc\]](#).
- [49] M. Boyle, D. Iozzo, and L. C. Stein, [moble/scri: v1.2](#) (2020).
- [50] J. Blackman, S. E. Field, M. A. Scheel, C. R. Galley, D. A. Hemberger, P. Schmidt, and R. Smith, A Surrogate Model of Gravitational Waveforms from Numerical Relativity Simulations of Precessing Binary Black Hole Mergers, *Phys. Rev. D* **95**, 104023 (2017), [arXiv:1701.00550 \[gr-qc\]](#).
- [51] G. B. Cook, Aspects of multimode Kerr ringdown fitting, *Phys. Rev. D* **102**, 024027 (2020), [arXiv:2004.08347 \[gr-qc\]](#).
- [52] L. London, D. Shoemaker, and J. Healy, Modeling ringdown: Beyond the fundamental quasinormal modes, *Phys. Rev. D* **90**, 124032 (2014), [Erratum: *Phys. Rev. D* **94**, 069902 (2016)], [arXiv:1404.3197 \[gr-qc\]](#).
- [53] V. Baibhav and E. Berti, Multimode black hole spectroscopy, *Phys. Rev. D* **99**, 024005 (2019), [arXiv:1809.03500 \[gr-qc\]](#).
- [54] E. Berti and A. Klein, Mixing of spherical and spheroidal modes in perturbed Kerr black holes, *Phys. Rev. D* **90**, 064012 (2014), [arXiv:1408.1860 \[gr-qc\]](#).
- [55] A. Dhani and B. S. Sathyaprakash, Overtones, mirror modes, and mode-mixing in binary black hole mergers, (2021), [arXiv:2107.14195 \[gr-qc\]](#).
- [56] E. Finch and C. J. Moore, Modeling the ringdown from

- precessing black hole binaries, *Phys. Rev. D* **103**, 084048 (2021), [arXiv:2102.07794 \[gr-qc\]](#).
- [57] A. Dhani, Importance of mirror modes in binary black hole ringdown waveform, *Phys. Rev. D* **103**, 104048 (2021), [arXiv:2010.08602 \[gr-qc\]](#).
- [58] K. Mitman *et al.*, Nonlinearities in Black Hole Ringdowns, *Phys. Rev. Lett.* **130**, 081402 (2023), [arXiv:2208.07380 \[gr-qc\]](#).
- [59] M. H.-Y. Cheung *et al.*, Nonlinear Effects in Black Hole Ringdown, *Phys. Rev. Lett.* **130**, 081401 (2023), [arXiv:2208.07374 \[gr-qc\]](#).
- [60] M. H.-Y. Cheung, E. Berti, V. Baibhav, and R. Cotesta, Extracting linear and nonlinear quasinormal modes from black hole merger simulations, *Phys. Rev. D* **109**, 044069 (2024), [arXiv:2310.04489 \[gr-qc\]](#).
- [61] C. Pacilio, S. Bhagwat, F. Nobili, and D. Gerosa, post-merger: A flexible mapping of ringdown amplitudes for non-precessing binary black holes, In prep.